

## An investigation of a biomass hydrogel electrolyte naturally stabilising cathodes for zinc-ion batteries

Haobo Dong<sup>a</sup>, Jianwei Li<sup>a</sup>, Siyu Zhao<sup>a</sup>, Yiding Jiao<sup>a</sup>, Jintao Chen<sup>a</sup>, Yesu Tan<sup>a</sup>, Dan J.L. Brett<sup>b</sup>, Guanjie He<sup>\*a, b, c</sup> and Ivan P. Parkin<sup>\*a</sup>

<sup>a</sup>Christopher Ingold Laboratory, Department of Chemistry, University College London, 20 Gordon Street, London WC1H 0AJ, U.K. Email: [g.he@ucl.ac.uk](mailto:g.he@ucl.ac.uk); [i.p.parkin@ucl.ac.uk](mailto:i.p.parkin@ucl.ac.uk)

<sup>b</sup>Electrochemical Innovation Lab, Department of Chemical Engineering, University College London, 20 Gordon Street, London WC1H 0AJ, U.K.

<sup>c</sup>School of Chemistry, University of Lincoln, Brayford Pool, Lincoln, LN6 7TS, UK.

**KEYWORDS:** zinc-ion batteries, flexible devices, hydrogel electrolytes, cathode stabilised electrolyte, biomass materials

---

**ABSTRACT:** Aqueous zinc-ion batteries (AZIBs) have the potential to be utilised in grid-scale energy storage system owing to their high energy density and cost-effective properties. However, the dissolution of cathode materials and the irreversible extraction of pre-intercalated metal-ions in the electrode materials restrict the stability of AZIBs. Herein, a cathode stabilised zinc-ion batteries (ZIBs) strategy is reported based on a natural biomass polymer sodium alginate as the electrolyte coupling with a Na<sup>+</sup> pre-intercalated  $\delta$ -Na<sub>0.65</sub>Mn<sub>2</sub>O<sub>4</sub>·1.31H<sub>2</sub>O cathode. The dissociated Na<sup>+</sup> in alginate after gelation directly stabilises the cathodes by preventing the collapse of layered structures during charge processes. The as-fabricated ZIBs deliver a high capacity showing 305 mAh g<sup>-1</sup> at 0.1 A g<sup>-1</sup>, even 10% higher than the ZIBs with an aqueous electrolyte. Further, the hybrid polymer electrolyte possessed excellent coulombic efficiency above 99% and capacity retention of 96% within 1000 cycles at 2 A g<sup>-1</sup>. A detailed investigation combining *ex-situ* experiments uncover the charge storage mechanism and the stability of assembled batteries, confirming the reversible diffusions of both Zn<sup>2+</sup> and pre-intercalated Na<sup>+</sup>. A flexible device of ZIBs fabricated based on vacuum-assisted resin transfer molding (VARTM) possesses an outstanding performance of 160 mAh g<sup>-1</sup> at 1 A g<sup>-1</sup>, which illustrates their potential for wearable electronics in mass production.

---

### Introduction

With increasing interest of wearable and implantable electronics in healthcare<sup>1</sup> and bendable displays<sup>2</sup>, flexible and biocompatible energy storage devices have attracted significant attention. Lithium-ion batteries (LIBs), a technology possessing high energy density<sup>3</sup>, dominated the energy storage sector for several decades<sup>4</sup>. However, the high cost (\$190/KWh)<sup>5</sup>, limited lithium resources, safety issues and the complex manufacturing conditions<sup>6</sup>, are barriers to uptake broader applications<sup>7,8</sup>. As an promising alternative secondary battery, the aqueous zinc-ion battery (AZIB) with mild acidic aqueous electrolyte, is the subject of intense interest attributing to its superior abundance, relatively low cost<sup>9</sup>, environmental benignity and less toxicity<sup>10</sup> compared to LIBs. Theoretically, zinc anodes offer a high gravimetric capacity of 820 mAh g<sup>-1</sup>, and a volumetric capacity of 5855 mAh cm<sup>-3</sup>.<sup>11</sup> The redox potential of Zn/Zn<sup>2+</sup> is -0.763 V versus standard hydrogen electrode (SHE), which is suitable for them to use in aqueous electrolyte system.

To date, cathode materials employed for AZIBs can be divided into four categories, manganese-based oxides<sup>12-14</sup>, vanadium-based oxides<sup>15-17</sup>, Prussian blue analogs<sup>18,19</sup> and other cathode materials including inorganic molybdenum sulphates<sup>20</sup>, molybdenum oxides<sup>21,22</sup>, and organic quinone compounds<sup>23,24</sup>. These materials function as the insertion host for AZIBs, where Zn<sup>2+</sup> ions with an ionic radius (0.74 Å) intercalate into the host

structure during the reversible charge/discharge process contributing to a high specific capacity. However, because of the repulsion of the electrostatic interaction between Zn<sup>2+</sup> ions and the cathode host, the insertion process is sluggish. Hence, guest species from metal ions with large ionic radius are pre-intercalated into the pristine cathode materials to expand the host channels for insertions. Concerning manganese-based oxides,  $\delta$ -MnO<sub>2</sub> exhibits the layered framework and is beneficial for the modification of pre-intercalated ions. However, during the charge process, the pre-intercalated ions are under the risk of releasing from the host and resulting in the collapse of structures. Wang *et al.*<sup>25-28</sup> made a significant contribution in Mn-based cathode materials. H<sup>+</sup> and Zn<sup>2+</sup> intercalation mechanism was proposed, and the as-prepared AZIBs delivered excellent specific capacity above 300 mAh g<sup>-1</sup>.

Polymer electrolytes in ZIBs, attracting considerable attention, can provide fast ion mobility and solve the safety issues by prohibiting the zinc dendrite penetrating through the separator thus to avoid the short circuit. Regarding the polymer electrolyte in a flexible device, additional mechanical properties of the polymer electrolyte offer the battery with robustness in bending, twisting and cutting tolerance. Previous studies dissolved zinc trifluoromethanesulfonate (Zn(CF<sub>3</sub>SO<sub>3</sub>)<sub>2</sub>) into the solid polymers polyethylene oxide (PEO)<sup>29</sup>, polyvinylidene difluoride (PVDF)<sup>30</sup>, polyacrylonitrile (PAN)<sup>31</sup> and poly(vinyl alcohol) (PVA)<sup>32</sup>, which delivered relatively low ionic conductivities

from  $10^{-4}$  to  $10^{-3}$  S  $\text{cm}^{-1}$ . It is generally agreed that conventional ion transportation in the polymer electrolyte occurs by segmental motion<sup>33</sup>. Similar to lithium-ion transportation in polymer electrolytes, zinc ions in the salt-polymer complex hop from one coordination site of a functional group to another one.<sup>34-36</sup> The low active segmental motion of  $\text{Zn}^{2+}$  ions among the covalent soft chains of solid organic polymer electrolytes results in low ionic conductivity, the inducing of water content, such as forming hydrogel electrolyte, in the polymer electrolyte becomes a prospective way. Recent progress in hydrogel electrolytes for ZIBs complies the advantage of aqueous ZIBs such as a high electron conductivity in the magnitude of  $10^{-2}$  S  $\text{cm}^{-1}$ ,<sup>37-39</sup> however, the ion transport mechanism in the hydrogel ZIBs has not been investigated in details. Zhi et al<sup>40-42</sup> indicated that increasing concentrated aqueous electrolytes in hydrogel electrolyte has profound influences on electrochemical stability. Furthermore, Liang et al<sup>43-48</sup> comprehensively investigated the mechanism in AZIBs, especially for electrolytes, indicating that a less water content could result from a higher interfacial charge transfer associated with activation energies and  $\text{Zn}^{2+}$  desolvation at the cathode interface. In addition, most of the previous work regarding polymer/solid-state electrolytes for different secondary batteries focused on the improvement of ion

transport, and the suppression of zinc dendrite for zinc anode<sup>49</sup>, whereas the influence of the electrode materials has been seldomly discussed.

Here, we introduce a robust and flexible ZIBs based on a cathode stabilised hydrogel electrolyte (CSHE) from sodium alginate, accompanying with a sodium pre-intercalated cathode material  $\delta\text{-Na}_{0.65}\text{Mn}_2\text{O}_4 \cdot 1.31\text{H}_2\text{O}$ . Attribute to the affinity of natural alginates, the alginate hydrogel electrolyte could form when divalent transition metals ions are replaced with  $\text{Na}^+$  ions, where the affinity is in the order of  $\text{Pb}^{2+} > \text{Cu}^{2+} > \text{Cd}^{2+} > \text{Ca}^{2+} > \text{Fe}^{2+} > \text{Ni}^{2+} > \text{Zn}^{2+} > \text{Mn}^{2+}$ .<sup>50</sup> The free dissociated  $\text{Na}^+$  ions in the hydrogel electrolyte prevent the irreversible loss of the pre-intercalated  $\text{Na}^+$  ions in the active materials, and further stabilise the layered structure to achieve an intrinsic specific capacity of 305 mAh  $\text{g}^{-1}$  at 0.1 A  $\text{g}^{-1}$ . To address the energy storage mechanisms of the superior biomass hydrogel ZIBs, the electrodes during cycling were investigated by multiple *ex-situ* characterisations confirming the reversible intercalations of  $\text{Zn}^{2+}$ , and  $\text{Na}^+$  ions. The as-prepared flexible device also exhibits an excellent stretchability.

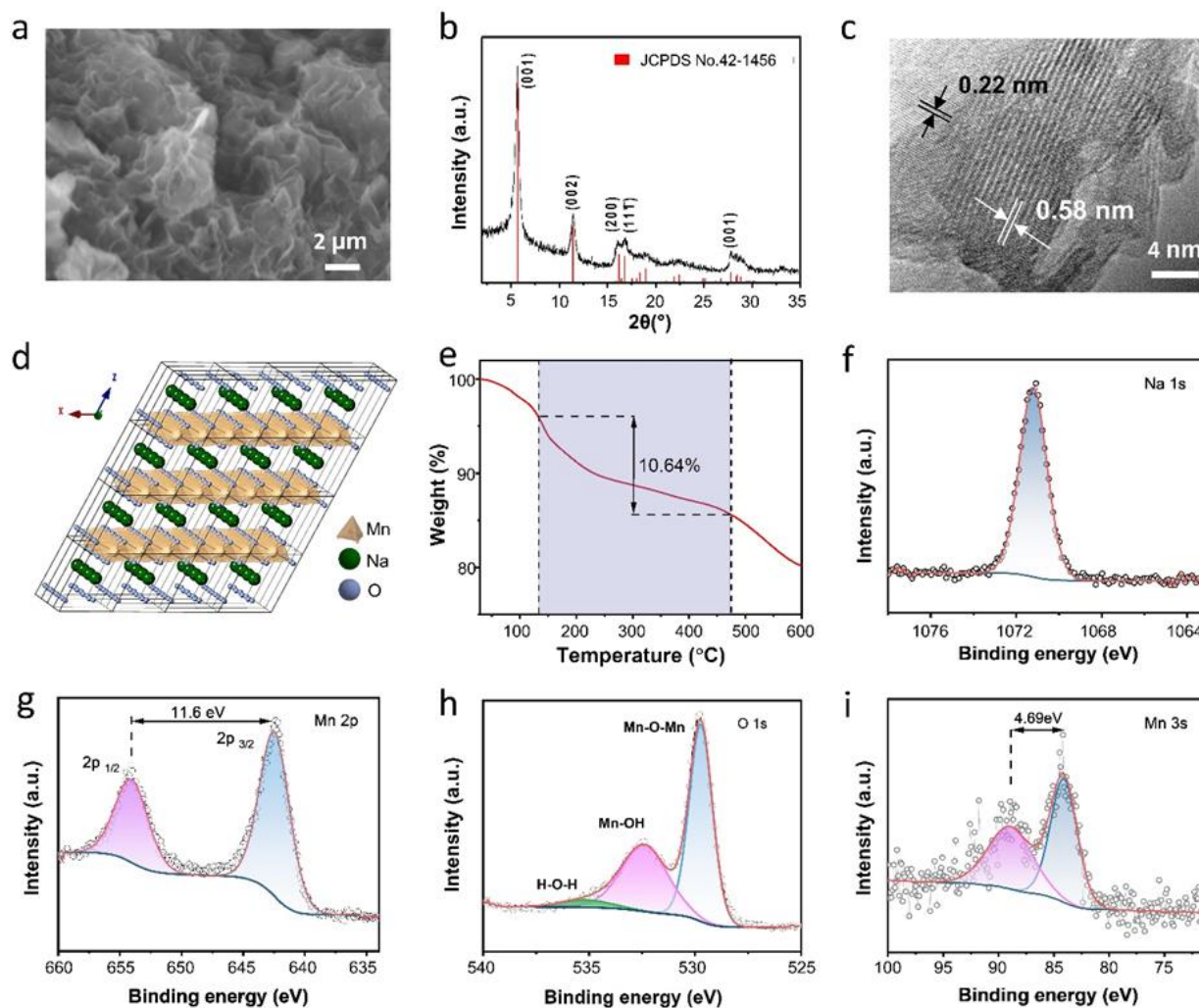


**Figure 1.** (a) SEM image; (b) XRD pattern; (c) TEM image of as-obtained  $\delta$ - $\text{Na}_{0.65}\text{Mn}_2\text{O}_4 \cdot 1.31\text{H}_2\text{O}$ , respectively; (d) Crystallographic structure of sodium pre-intercalated  $\text{MnO}_2$ . (Z-axis is perpendicular outwards); (e) TGA results with the temperature up to 600°C; (f), (g), (h) and (i) XPS spectra for Na 1s, Mn 2p, O 1s and Mn 3s, respectively.

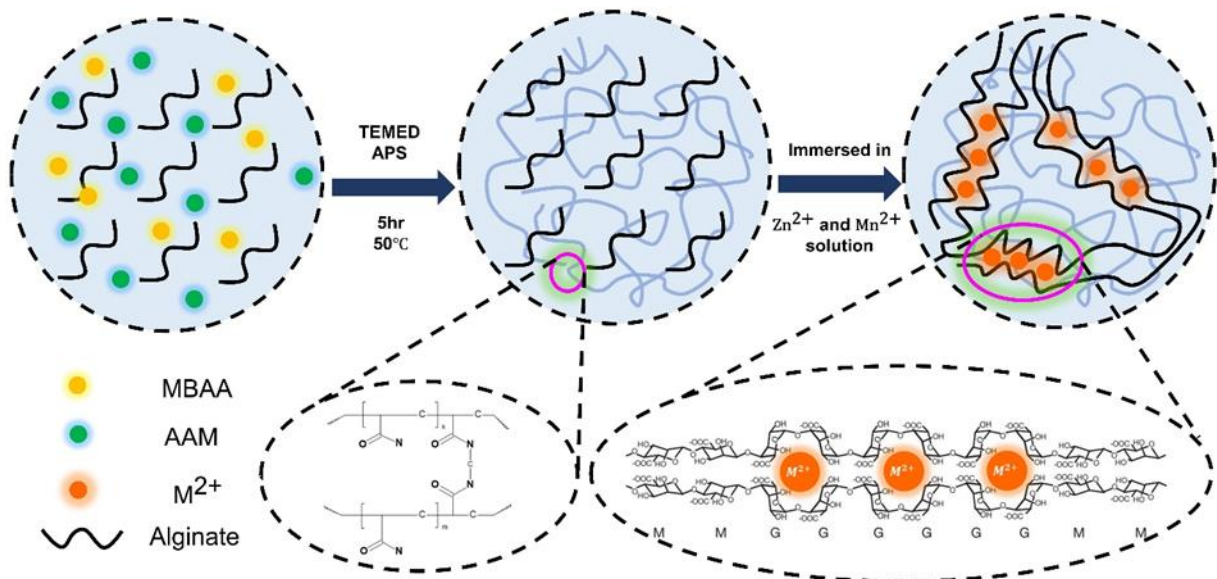


**Figure 2.** Schematic diagram of the synthetic route of the hybrid polymer electrolyte SA-PAM in three steps. PAM is firstly polymerised by free radical polymerisation forming covalent crosslinking. The gelation of alginate by ionic bonding generates the egg-box shaped structure

## Results and discussion

Hydrated sodium pre-intercalated  $\delta$ - $\text{MnO}_2$  (NMO) was synthesised by a facile co-precipitation method (details in Supporting Information) and utilised as the active material for the cathode. Scanning electron microscopy (SEM) image (Figure 1a) presents the morphology of the  $\text{Na}_n\text{Mn}_2\text{O}_4$  where microscale irregular nanosheets are attained. The X-ray diffraction (XRD) pattern exhibited in Figure 1b coincides well with Birnessite  $\text{Na}_{0.55}\text{Mn}_2\text{O}_4 \cdot 1.5\text{H}_2\text{O}$  (JCPDS no. 43-1456), where  $a = 5.175(3)$  Å,  $b = 2.849(1)$  Å,  $c = 7.338(5)$  Å,  $\alpha = \gamma = 90^\circ$  and  $\beta = 103.19(4)^\circ$ ,  $V = 105.3(6)$  Å<sup>3</sup>. The compositional ratio between pre-intercalated Na and Mn determined from the energy-dispersive X-ray spectroscopy (EDS) (Figure S2) is 0.327, hence the molecular formula is  $\text{Na}_{0.65}\text{Mn}_2\text{O}_4$  with an average oxidation state of 3.67 for Mn. Figure S2 also clarifies the homogeneity of the elements Na, Mn and O for the as-obtained cathode materials. Transmission electron microscopy (TEM) was characterised to determine the interlayer spacing and the nanostructure. As shown in Figure 1c, the d-space of the interlayer is 2.22 Å, which is close to the XRD pattern showing the lattice plane of (201). Meanwhile, with the pillars of  $\text{Na}^+$  ions and crystal waters, the measured interlayer spacing is 0.58 nm, which is conducive to ion intercalation. Extra TEM images shown in Figure S11 also reveal the similar interlayer spacing. The detailed crystal structure in Figure 1d reveals that the  $\text{Na}^+$  and water molecules are positioned between the Mn-O sheet, in which each Mn atom connects with six O atoms forming the octahedra structure. The number of crystal water molecules hydrated in  $\text{Na}_{0.65}\text{Mn}_2\text{O}_4$  was determined by the thermogravimetric analysis

(TGA) (see Figure 1e). The highlighted region is where the crystal water sublimed from 120 to 480°C, and the 10.64% weight loss corresponds to 1.31 water molecules, hence the as-prepared cathode material is  $\text{Na}_{0.65}\text{Mn}_2\text{O}_4$ , matching well with the standard XRD pattern (JCPDS no. 43-1456). X-ray photoelectron spectroscopy (XPS) was utilised to investigate the average oxidation state (AOS) of each element on the surface of the material. Na is observed as shown in Figure 1f (Na 1s) with a characteristic peak at 1071 eV. Mn 2p has two separate peaks with the binding energy difference of 11.6 eV, whereas the difference is 4.69 eV for Mn 3s spectrum. Based on the binding energy difference of the Mn 3s peak, the average oxidation state of Mn is calculated to be 3.68 according to the formula  $\text{AOS} = 8.956 - 1.126\Delta E_s$ <sup>51</sup>, where the Mn valence state is close to the value deduced from the elemental composition. In terms of O 1s (Figure 1h), the spectrum is convoluted from three corresponding peaks which are assigned to adsorbed water H-O-H (533.4 eV), surface adsorbed oxygen ions Mn-OH (532.2 eV) and lattice oxygen species Mn-O-Mn (529.8 eV), respectively.<sup>52</sup>

To stabilise the active materials in cathodes, a cathode stabilised hydrogel electrolyte (CSHE) was developed based on a biomass material sodium alginate (SA). Sodium alginate is the most commercial alginic acid salt refined from brown seaweeds. It is comprised of mannuronic acid (M unit) and gulonic acid (G unit), arranging in blocks rich in G units, blocks rich in M units, and blocks of alternating G and M units. In an aqueous solution, the G blocks in different alginate chains form ionic crosslinks through divalent cations resulting in a network of alginate hydrogel.<sup>53</sup> The gelation mechanism is beneficial for

polymer electrolyte utilised in ZIBs, where hydrogel electrolyte is generated when sodium alginate reacts with  $Zn^{2+}$  or  $Mn^{2+}$ .  $Na^+$  ions dissociated in the hydrogel alleviate the decomposition of the cathode material  $Na_{0.65}Mn_2O_4 \cdot 1.31H_2O$  naturally during charging process resulting in a high capacity similar to the theoretical value of  $\delta-MnO_2$ . Covalent crosslinking polyacrylamide (PAM) is incorporated into the hydrogel electrolyte enhancing the polymeric framework, the additional covalent bonds offer a robust 3D porous structure for the hierarchical hydrogel electrolyte sodium alginate-polyacrylamide (SA-PAM). The biomass hydrogel electrolyte was synthesised in three steps (Figure 2) by combining alginate and polyacrylamide to form a co-polymer. Pristine sodium alginate (SA) was firstly dissolved into the deionised water under intensive stirring before adding the acrylamide (AAM) monomer, obtaining a light brown homogeneously mixed solution. The crosslinker N,N'-methylenebisacrylamide (MBAA), the photo-initiator ammonium persulfate (APS) and the accelerator N,N,N',N'-tetramethylethylenediamine (TEMED) were added into the mixture sequentially with continuous stirring for 30 min. The homogeneous mixture was then poured into a glass Petri dish followed by rad-

ical polarisation at 5°C for 5 hours where upon a polyacrylamide hydrogel film was formed by molecular level covalent crosslinkings. Eventually, the network of alginate in the sodium alginate-polyacrylamide (SA-PAM) hydrogel was formed by immersing the well-prepared film into a solution of 1 M  $ZnSO_4$  and 0.2 M  $MnSO_4$  for 24 hours ensuring alginate G blocks to form gelation with divalent cations in the aqueous salt solution. Due to the metal ions affinity to the carboxylic acid,  $Na^+$  was replaced by the divalent cations. Negatively charged carboxylic acid  $-COO^-$  groups from the G blocks facilitate ionic bonding with  $Zn^{2+}$  and  $Mn^{2+}$  forming an egg-box shaped structure connecting two alginate chain together. Hydrophilic pendant groups of alginate and polyacrylamide attract and absorb the water molecules by dipole-dipole bonding. Hence, the light transparent alginate polyacrylamide co-polymer electrolyte (see Figure 3a) with two polymer crosslinks referred to as SA-PAM was fabricated. As for comparison, a pristine sodium alginate polymer electrolyte film referred to as SA, was fabricated by a simple evaporating process at 40°C followed by the immersing process as illustrated above.

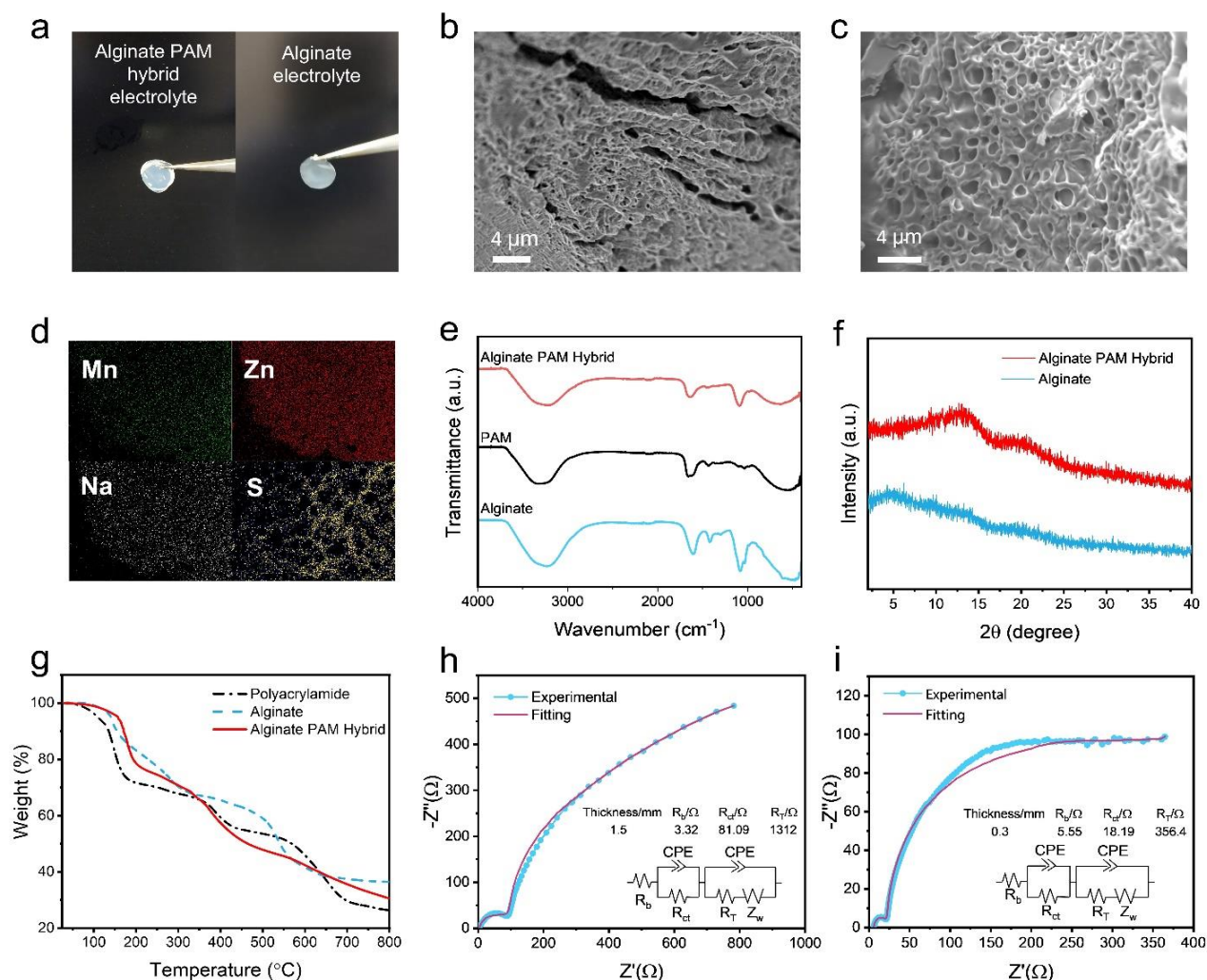


**Figure 3** (a) Optical photos for both hybrid and pristine alginate electrolytes; (b) SEM of pristine SA polymer electrolyte; (c) SEM of hybrid SA/PAM polymer electrolyte; (d) EDS mapping of hybrid SA-PAM; (e) FTIR spectra; (f) XRD patterns; (g) TGA analysis; (h) EIS results for SA-PAM under full cell evaluation using a  $Na_{0.65}Mn_2O_4$  cathode; (i) EIS results for SA under full cell test using a  $Na_{0.65}Mn_2O_4$  cathode

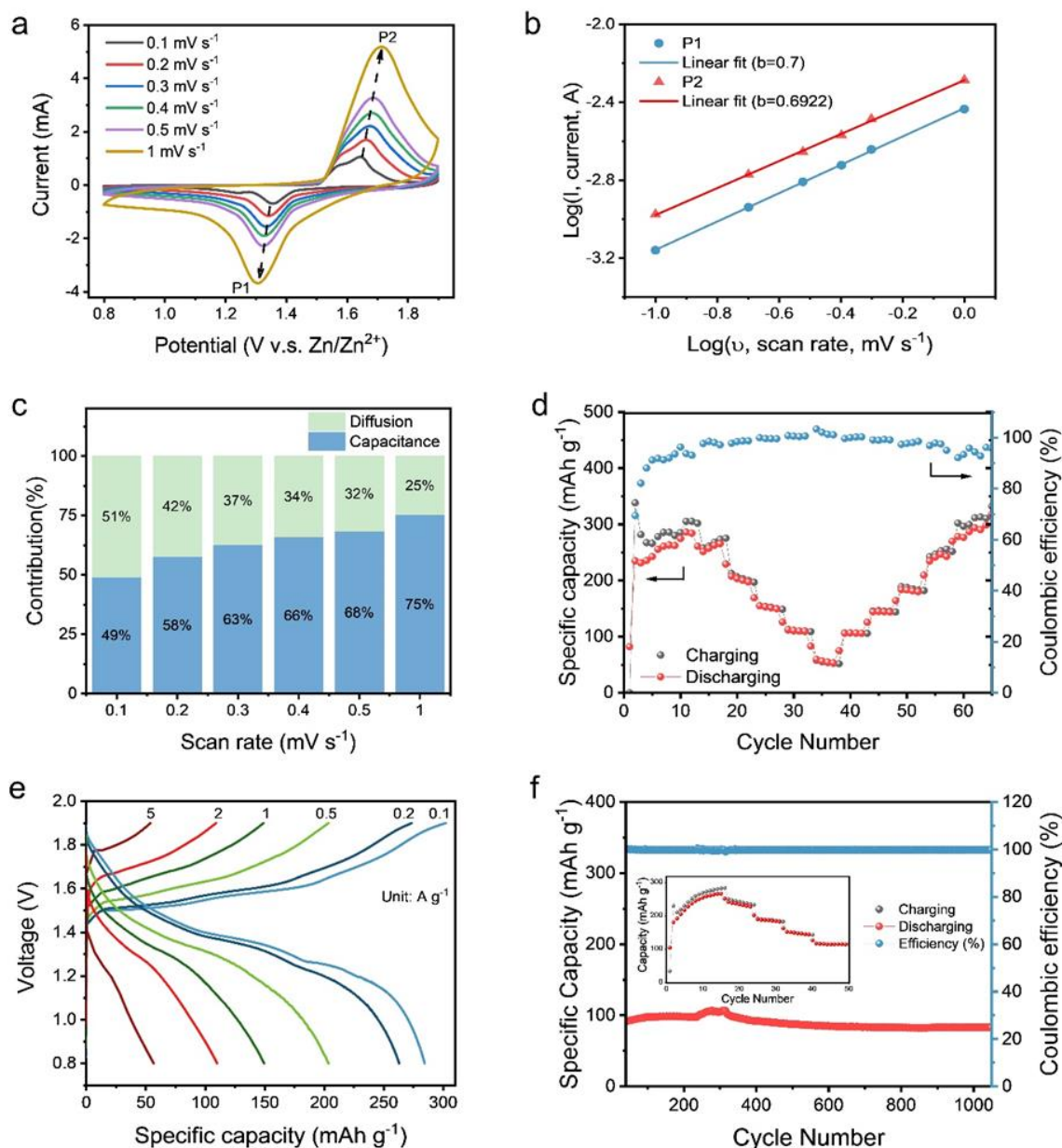


**Figure 4** SA-PAM electrolyte under full cell test. (a) CV curves scan rates ranging from 0.1  $\text{mV s}^{-1}$  to 1  $\text{mV s}^{-1}$ ; (b) diffusion-capacitive contribution with  $\log(i)$  vs  $\log(v)$  plots of two peaks in CV curves; (c) diffusion-capacitive control contribution presented in the bar chart; (d) Charge/discharge rate performance of current densities from 0.1 to 5  $\text{A g}^{-1}$ ; (e) Galvanostatic charge/discharge profiles for SA-PAM-NMO full cell at different current densities; (f) Long-term cycling stability under the current density of 2  $\text{A g}^{-1}$ . The insert plot is the activation process for the first 50 cycles.

In terms of microstructures, although the optical images of SA-PAM and SA have a similar appearance as light-transparent films (Figure 3a), the SEM images reveal that the copolymer SA-PAM possesses a highly porous 3D structures (Figure 3c) compared with less porous structures for the pristine SA electrolyte film (Figure 3b). The porous architecture enables a higher aqueous solution absorption, which may increase the ionic conductivity and mechanical tensile strain ability. The EDS mapping (Figure 3d) reveals that the SA-PAM electrolyte is homogenous under the synthetic method demonstrated above. XPS results (Figure S3) provide further evidence of the ele-

ments present on the surface of the hydrogel, for which dissociated  $\text{Na}^+$  is detected. Fourier-transform infrared spectroscopy (FTIR) was utilised (Figure 3e) to exploit the polymerisation mechanism. As for alginate, the characteristic absorption peaks at 1600  $\text{cm}^{-1}$  and 1420  $\text{cm}^{-1}$  represent asymmetric and symmetric  $-\text{COO}^-$  stretching owing to the  $\text{Zn}^{2+}$  and  $\text{Mn}^{2+}$  cations. Bands at 1298  $\text{cm}^{-1}$  for C-H deformation, and the other sharp bands at 1076  $\text{cm}^{-1}$  and 1030  $\text{cm}^{-1}$  are assigned for C-O stretching in CH-OH and C-O-C structures, respectively. With regard to PAM, two separate bands at 1649  $\text{cm}^{-1}$  and 1429  $\text{cm}^{-1}$  are for N-H bending and C-N stretching in  $-\text{CO-NH}-$ . The band at 1670  $\text{cm}^{-1}$

<sup>1</sup> should be C=O stretching and the NH<sub>2</sub> in-plane rocking is detected at 1113 cm<sup>-1</sup>. As for the co-polymer SA-PAM, after adding PAM to sodium alginate, the broad bands around 3200 cm<sup>-1</sup> for both hybrid polymer SA-PAM and PAM represent the combination of O-H and N-H stretching vibration, while for pristine alginate, only O-H stretching should be observed and the band shift to 3300 cm<sup>-1</sup>. The hybrid polymer possesses the peaks for both SA and PAM, while transmittances of C-O stretching at 1085 cm<sup>-1</sup>, N-H bending at 1647 cm<sup>-1</sup> and C-N stretching at 1427 cm<sup>-1</sup> are all reduced compared with the pristine electrolyte. Regarding the XRD spectrum (Figure 3f), the broad reflection observed instead of the characteristic reflections for both alginate and the hybrid SA-PAM reveals that most regions of those polymer electrolytes are in the amorphous state. Thermal stabilities of the SA and hybrid SA-PAM were determined by TGA from 25 to 800°C at a rate of 10°C min<sup>-1</sup>. As displayed in Figure 3g, there are three pyrolysis stages for the thermal degradation process for both pristine and hybrid polymers. However, the first stage degradation temperature of hybrid SA-PAM is 155°C which is higher than that of SA (120°C) and PAM (110°C). The combination of ionic and covalent crosslinking process improves the thermal stability of the polymers. The ionic conductivities and inherent resistance shown in Figure 3h and 3i were investigated by electrochemical impedance spectroscopy (EIS). According to the bulk resistance ( $R_b$ ) of the polymer internal resistance, even pristine alginate polymer electrolyte storing Zn<sup>2+</sup> in the “egg box” structure achieves a high ionic conductivity of 3.51×10<sup>-3</sup> S cm<sup>-1</sup>. Complexing with PAM, the hybrid SA-PAM exhibits a relatively higher ionic conductivity of 2.92×10<sup>-2</sup> S cm<sup>-1</sup>, which could result in the 3D hierarchical architecture provided by PAM expanding the free volumes for ion transportation.

Cyclic voltammetry (CV) of the hybrid SA-PAM exhibited in Figure 4a was analysed under different scan rates from 0.1 mV s<sup>-1</sup> to 1 mV s<sup>-1</sup>. At a lower rate of 0.1 mV s<sup>-1</sup>, two pairs of reduction and oxidation peaks are observed, with reduction peaks at 1.36 and 1.23 V; and oxidation peaks at 1.57 and 1.64 V. With increasing the scan rates, two pairs of redox peaks overlap to a single pair of redox peaks at a higher rate at the voltage of 1.3 and 1.65 V. Comparing with pristine alginate electrolyte SA (Figure S5a), it also maintains the same redox peaks located at the same potentials. To further investigate the kinetic process regarding different electrolytes to the cathode material, diffusion-controlled and capacitive contribution of SA-PAM were evaluated based on two peaks as shown in Figure 4a. Calculations are described in the supporting information.

As presented in Figure 4c, the electrochemical reaction is more reliant on capacitive control when the sweep rate increases from 0.1 to 1 mV s<sup>-1</sup>. Considering the pristine alginate SA, the kinetic process is dominated by the diffusion-controlled process with  $b$  values of 0.66 and 0.69 (Figure S5b). However, as the sweep rate increasing, the entire battery is more affected by the capacitive control, which is consistent with the results of SA-PAM (see Figure S5c). Compared with the aqueous battery, CV

rate experiments for the AZIBs were also investigated with the same cathode material Na<sub>0.65</sub>Mn<sub>2</sub>O<sub>4</sub>·1.31H<sub>2</sub>O and an aqueous electrolyte of 1M ZnSO<sub>4</sub> and 0.2M MnSO<sub>4</sub> solution. Results (Figure S6c) demonstrate that the aqueous battery is mainly influenced by capacitive control, which is the same as the hybrid SA-PAM batteries. With the increase of hydroxylic groups in the hybrid polymer, SA-PAM is more hydrophilic than the pristine SA and the hybrid electrolyte SA-PAM exhibits a similar capacitive performance to the aqueous battery. Charge/discharge rate performances of SA-PAM, SA and aqueous ZIBs, displayed in Figure 4d, S5d and S6d, respectively, were investigated under stepwise current densities from 0.1 to 5 A g<sup>-1</sup> with 5 cycles for each current density. Impressively, the SA-PAM battery could achieve 305 mAh g<sup>-1</sup> at 0.1 A g<sup>-1</sup> with an outstanding coulombic efficiency (CE) of 96.2 % compared to 258 mAh g<sup>-1</sup> with 91.6% coulombic efficiency (CE) for the pristine SA battery (see Figure S5d). The rate performance of the hybrid hydrogel battery was measured at current densities of 0.1, 0.2, 0.5, 1, 2, 5 A g<sup>-1</sup> and exhibiting a good recovery ability with 305, 273, 203, 152, 110 and 55 mAh g<sup>-1</sup>, respectively. The specific capacity of SA-PAM at a low current rate (0.1 A g<sup>-1</sup>) is 10% higher than the aqueous battery (277 mAh g<sup>-1</sup>), whereas the values of SA-PAM at a higher current density (5 A g<sup>-1</sup>) is 22% lower than that of the aqueous battery (70.6 mAh g<sup>-1</sup>). These differences could be attributed to the interfacial effect and the dissolution of cathode materials in aqueous solutions. A benefit of the solid-solid interface between cathode and electrolyte is that the dissolution of the cathode material into the aqueous electrolyte is inhibited by the hydrogel electrolyte. Meanwhile, the dissociated Na<sup>+</sup> ions in the hydrogel electrolyte stabilise the crystal structure of the active material preventing the permanent deintercalation of the Na<sup>+</sup> ions into the electrolyte, hence offering a high capacity compared with the AZIBs at a lower current density. At a higher current density, the incomplete chemical reaction at the solid-solid interface results a less ion transportation compared to the reaction in the aqueous solution, hence resulting in a relatively lower capacity.

Galvanostatic charge/discharge profiles for SA-PAM at different current densities are illustrated in Figure 4e. During the discharge process at 0.1 A g<sup>-1</sup>, the first plateau positioned at 1.4 V is attributed to H<sup>+</sup> insertion; and the second plateau around 1.2 V is attributed to Zn<sup>2+</sup> insertion<sup>38</sup>. For the charging process, corresponding deintercalations of H<sup>+</sup> and Zn<sup>2+</sup> are assigned to the plateau at 1.55 V and 1.7 V. Both the pristine and hybrid hydrogel electrolyte batteries possess the plateaus at the same voltages as the aqueous battery, which implies that there is no obvious ion-transport reduction by utilising these hydrogels even for the pristine alginate (Figure S5e and S6e). Long-term cycling stability was determined under 2 A g<sup>-1</sup> for SA-PAM, SA and aqueous batteries (see Figure 4f, S5f and S6f) accompanying with the electrolyte 3M ZnSO<sub>4</sub> and 0.2M MnSO<sub>4</sub>. An activation applied at the beginning of the cycling test is to entirely polarise the solid-solid interface between the cathode and hydrogel electrolyte SA-PAM exhibited a superior

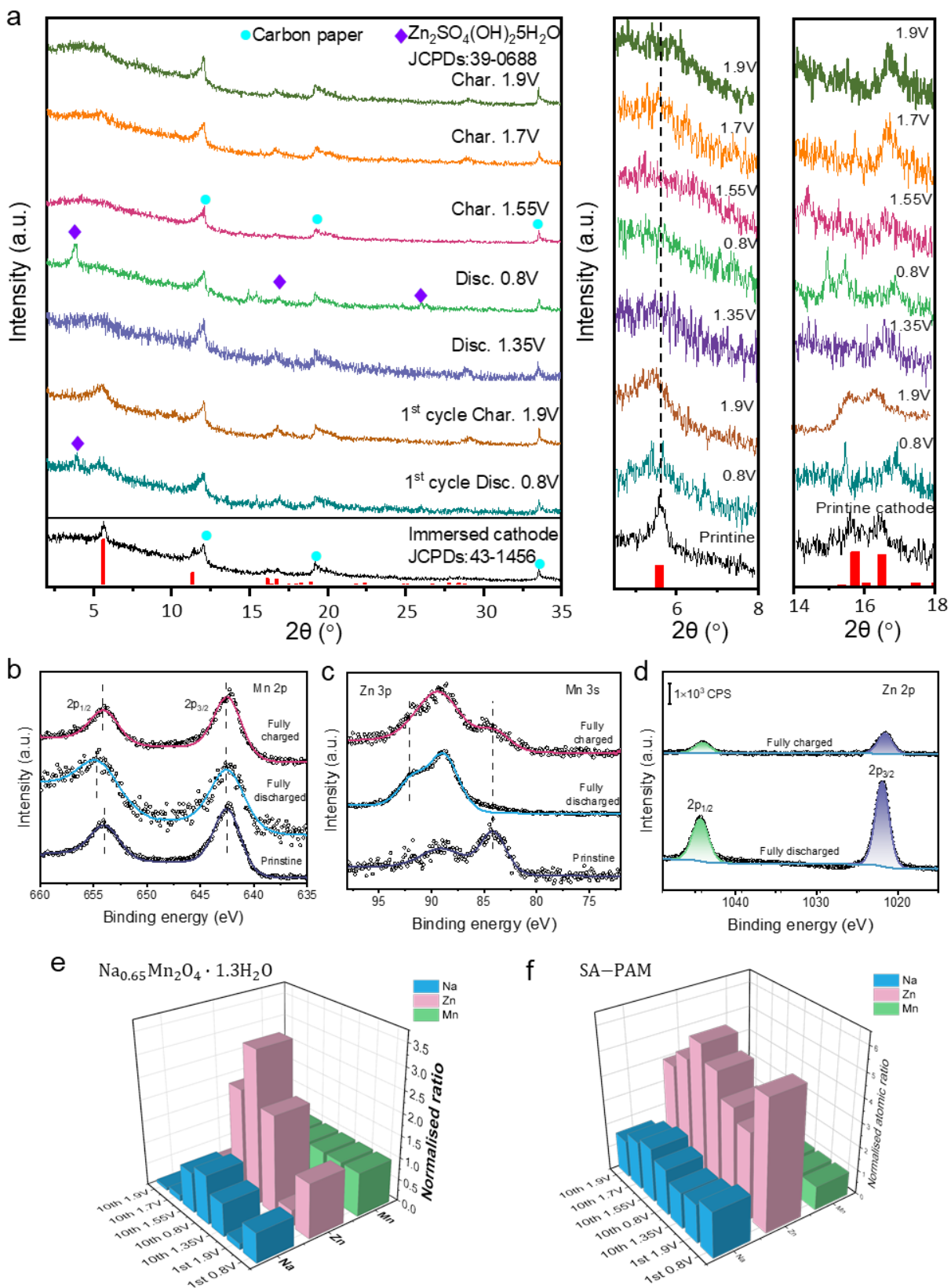


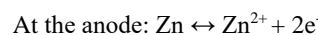
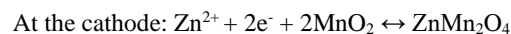
**Figure 5** (a) *Ex-situ* XRD spectra for the Na<sub>0.65</sub>Mn<sub>2</sub>O<sub>4</sub>·1.31H<sub>2</sub>O cathode under the full cell assembly with SA-PAM at different states of charge/discharge. Right two plots are amplified plots for peak (001); and (200) and (001); (b), (c), (d) *ex-situ* XPS spectra for Mn 2p, Mn 3s and Zn 2p respectively at fully charged and discharged states; (e) EDS results of elemental compositions with normalised ratios (with respect to Mn) for cathode material NMO; (f) EDS results of elemental compositions normalised with respect to Mn for polymer electrolyte SA-PAM.

capacity retention of 96% over 1000 cycles comparing with 70.1% capacity retention for pristine SA and 92% for aqueous electrolyte. Because of the weak electrostatic attraction-ionic bonding and the low ionic conductivity of SA, pristine SA electrolyte is not sufficient stable to reach a high capacity close to the intrinsic value. The fluctuation appeared in these figures are influenced by the ambient temperature change. Zn plating/stripping performance of the Zn//Zn symmetric cell shown in Figure S8 also indicates the stability with respect to aqueous electrolyte. SA-PAM maintains a stable performance throughout the 250-hour test, whereas the aqueous electrolyte could only keep 130 hours. As to verify the stabilising effect of additional Na<sup>+</sup> ions from alginate-PAM hydrogel electrolyte, both CV and cycling tests have performed under the electrolyte 3M ZnSO<sub>4</sub> 0.2MnSO<sub>4</sub> and 0.2 Na<sub>2</sub>SO<sub>4</sub>. As shown in the CV plot (Figure S15a), there is no additional redox peaks compared with SA-PAM and aqueous ZIBs (See Figure 4a and Figure S6a respectively). Regarding the charge/discharge cycling performance, the battery with additional sodium salt delivers a capacity retention of 95.2% (Figure S15b), greater than the one without sodium salt.

Combined *ex-situ* XRD, XPS and SEM-EDS analysis were performed to investigate the energy storage mechanism for the hydrogel ZIBs at the specific voltage as shown in Figure S13. Crystal structural evolution of Na<sub>0.65</sub>Mn<sub>2</sub>O<sub>4</sub> in the hydrogel ZIB was investigated by *ex-situ* XRD measured at specific state of charge (SOC) from 0.8 V to 1.9 V for the 1<sup>st</sup> and 10<sup>th</sup> cycles under the current density of 0.1 A g<sup>-1</sup>. According to the XRD patterns shown in Figure 5a, there is no significant phase variation during the charge/discharge processes, besides only 1° peak shift at the characteristic peak (001) and peak (11 $\bar{1}$ ). Although a small phase shift is observed, the entire layered structure remains stable during the charge/discharge process. Owing to Zn<sup>2+</sup> intercalation/deintercalation mechanism, intensity of these characteristic peaks is reduced during cycling. However, because of the Na<sup>+</sup> from the biomass sodium alginate, there is a supplement of Na<sup>+</sup> for the pre-intercalated  $\delta$ -Na<sub>0.65</sub>Mn<sub>2</sub>O<sub>4</sub>·1.31H<sub>2</sub>O during cycling. Therefore, these characteristic peaks can still be recognized after 10 cycles for SA-PAM comparing with the *ex-situ* spectra for aqueous ZIBs shown in Figure S14, where the peak (001) has almost disappeared at 10<sup>th</sup> cycle at 1.9V. Similar to aqueous ZIBs, the flower-like Zn<sub>4</sub>SO<sub>4</sub>(OH)<sub>6</sub>·5H<sub>2</sub>O is observed from SEM images (Table S1), while the depositions disappear during the charging process, which reveals the reversible Zn<sup>2+</sup> intercalations. Quantitative analysis of EDS also reveals reversible ion transportations in cathodes (Figure 5e), where the contents of both Na<sup>+</sup> and Zn<sup>2+</sup> increase in the discharge process and decrease in the charge process. Under the same electric field, Na<sup>+</sup> in the biomass electrolyte simultaneously insert into the cathode with Zn<sup>2+</sup> serving as the supplement to the pre-intercalated Na<sup>+</sup> in the cathode suppressing the Na<sup>+</sup> extraction during charging/discharge. Theoretically, the amount of Na<sup>+</sup> and Zn<sup>2+</sup> in the hydrogel electrolyte SA-PAM (Figure 5f) is expected in contrast with the cathode. However, because of the abundant Na<sup>+</sup> and Zn<sup>2+</sup> exhibited in the electrolyte, there is no notable intensity variation during the charge/discharge processes. Dissociated Na<sup>+</sup> in the hydrogel stabilises the cathode material by intercalating into the interlayer, hence avoiding the collapse of the crystal structure. Regarding the spectra of Mn 2p (Figure 5b), there is

a 1.0 eV peak shift for the doublet peak at the binding energy of 665.0 eV from fully discharged state to fully charged state. Spectra of Mn 3s is used to determine the variation of average oxidation state of Mn during cycling, whereas the overlaps of Zn 3p at 80-95 eV make it complicated to identify the exact valence state. However, the disappearance of the characteristic peak at 84 eV of Mn 3s in the fully discharged state confirms the oxidation state change of Mn during the charging/discharge process. The profile of Zn 2p in Figure 5e provides the evidences of formation of Zn<sub>4</sub>SO<sub>4</sub>(OH)<sub>6</sub>·5H<sub>2</sub>O where the area enclosed by the Zn 2p 3/2 peak (1022.2 eV) in the fully discharged state is greater than that in the fully discharged state (1021.6 eV).

Therefore, the chemical reaction could be illustrated as below by combining the intercalation and chemical conversion reactions.



Encouraged by the impressive cathode stabilised hydrogel properties, a flexible device was fabricated based on the vacuum-assisted resin transfer moulding (VARTM) technique<sup>54,55</sup>. This approach lends itself to scale-up from the experimental demonstrator to the industrial mass production. Carbon fibre fabrics were selected as the current collector to provide flexibility. Each layer as shown in Figure 6a was assembled using a simple lamination process. However, aiming to apply the VARTM and avoid short-circuit, a layer of filter paper was infused into the polymer electrolyte inserted between the electrodes. When the vacuum was applied, the hydrogel electrolyte SA-PAM was fully immersed through the electrodes and filled the entire battery. A layer of peel ply and breather were positioned on top of the laminates assembly to provide extra air vent for the assembled batteries. The rest process for polymerisation is the same as illustrated in Figure 2. The length of the resultant device is approximately 7 cm, which is of a scale suitable for portable electronic devices. By way of demonstration, connecting two devices in series, a light-emitting diode (LED) display panel can be powered by the device (Figure 6b). As demonstrated in Figure 6c, the 1.39V open-circuit potential of the flexible ZIB is the same as the coin cell assembly, which supports the approach as a suitable fabrication strategy. In order to demonstrate physical robustness of the device, the flexible ZIBs were connected to a digital temperature and humidity meter to act as an electrical load and subjected to mechanical stress. Bending, twisting and cutting was performed (Figure 6f, 6g and 6h), and the ability to power the meter was unaffected. To further assess the device's electrochemical performance, a galvanostatic charge/discharge experiment was performed (Figure 6b). At a current density of 1 A g<sup>-1</sup>, a surprisingly high specific capacity of 160 mAh g<sup>-1</sup> was obtained for a device-level demonstrator and is of a consistent level to that obtained from coin cell testing (Figure 4d). Tensile test proceeded (see Figure S9) also indicates an excellent stretchability for the hydrogel electrolyte. A SA-PAM with carbon fabrics composite was mechanically robust and electrochemically reliable. Supplementary Videos attached further demonstrate the device's physical flexibility and robustness.

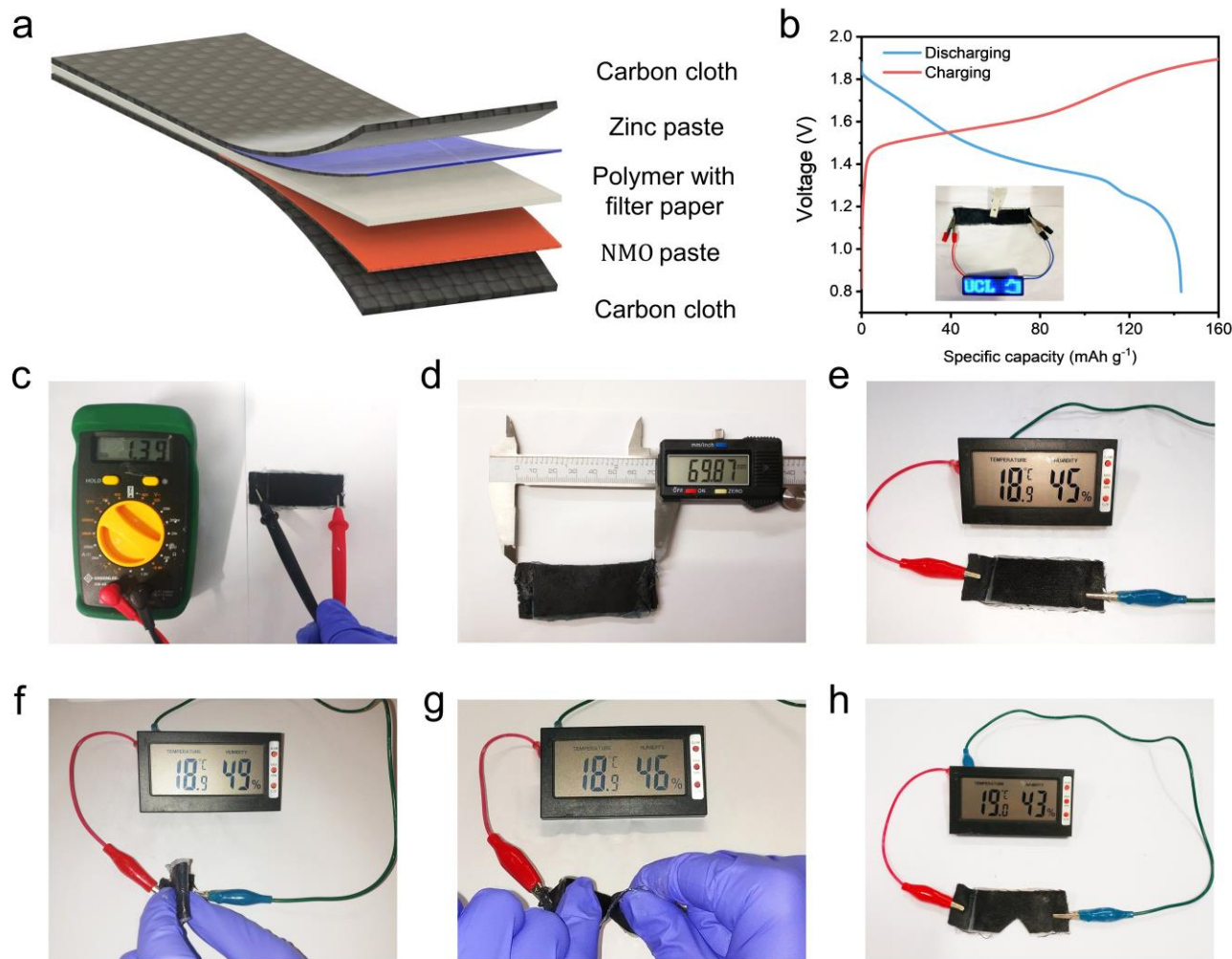


**Figure 6** (a) Schematic illustration of the flexible device; (b) galvanostatic charge-discharge results of the flexible device at a current density of  $1 \text{ A g}^{-1}$ . The internal graph shows the LED board powered by the devices connected in series; (c) open-circuit potential of the as prepared device; (d) dimension of the device; (e) initial state of the device which can power a digital temperature-humidity meter; (f) bending the device; (g) twisting the device; (h) cutting the device.

## Conclusion

A cathode-stabilised hydrogel-state ZIB was fabricated by combining a layered  $\delta\text{-Na}_{0.65}\text{Mn}_2\text{O}_4 \cdot 1.31\text{H}_2\text{O}$  and a cathode-stabilised hydrogel electrolyte (CSHE). The pristine biodegradable alginate electrolyte SA exhibits a specific capacity of  $258 \text{ mAh g}^{-1}$ , while the hybrid hydrogel electrolyte SA-PAM further enhances the electrochemical stability and mechanical properties, offering the a superior specific capacity and ionic conductivity of  $305 \text{ mAh g}^{-1}$  and  $2.92 \times 10^{-2} \text{ S cm}^{-1}$ , respectively. The *ex-situ* tests in XRD, XPS and EDS employed precisely investigate the electrochemical reactions for hydrogel ZIBs. The reversible intercalations of  $\text{Zn}^{2+}$  and  $\text{Na}^+$  observed on the cathode materials reveal that dissociated  $\text{Na}^+$  in the hydrogel electrolyte alleviate the collapse of the active material's crystal structure, thus offering a superior specific capacity. The fabricated flexible device also possesses a specific capacity of  $160 \text{ mAh g}^{-1}$  under  $1 \text{ A g}^{-1}$ , as well as superior mechanical properties being resistant to binding, twisting and cutting.

## ASSOCIATED CONTENT

## Supporting Information

Supporting Information Available: Experimental details of material fabrication and characterisation, additional SEM-EDS results, additional XPS spectra, additional CV and EIS profile of symmetric cell Zn//Zn, electrochemical performance for pristine SA and aqueous ZIBs, Zn plating/ stripping performance of the symmetric cell, tensile test of the flexible device, additional XRD spectrum, additional TEM images, *ex-situ* SEM-EDS results for cathode and the hydrogel electrolyte, a table of recent hydrogel electrolytes for ZIBs, and the video demonstrating the flexibility of the device fabricated.

## ACKNOWLEDGMENT

The authors would like to thank Engineering and Physical Sciences Research Council (EPSRC, EP/L015862/1, EP/R023581/1), STFC Batteries Network (ST/R006873/1), RSC Mobility Grant (M19-7656) for funding support and China Scholarship Council/University College London for the joint PhD scholarship.

## ABBREVIATIONS

CSHE: cathode-stabilised hydrogel electrolyte

## REFERENCES

- (1) Lee, G. H.; Moon, H.; Kim, H.; Lee, G. H.; Kwon, W.; Yoo, S.; Myung, D.; Yun, S. H.; Bao, Z.; Hahn, S. K. Multifunctional Materials for Implantable and Wearable Photonic Healthcare Devices. *Nat. Rev. Mater.* **2020**, *5* (5), 149–165. <https://doi.org/10.1038/s41578-019-0167-3>.
- (2) Myny, K. The Development of Flexible Integrated Circuits Based on Thin-Film Transistors. *Nat. Electron.* **2018**, *1* (1), 30–39. <https://doi.org/10.1038/s41928-017-0008-6>.
- (3) Kim, T.; Song, W.; Son, D. Y.; Ono, L. K.; Qi, Y. Lithium-Ion Batteries: Outlook on Present, Future, and Hybridized Technologies. *J. Mater. Chem. A* **2019**, *7* (7), 2942–2964. <https://doi.org/10.1039/C8TA10513H>.
- (4) Armand, M. Nature Lithium Battery. *Nature* **2001**, *414* (November), 359–367. <https://doi.org/10.1038/35104644>.
- (5) Frith, J. Lithium-Ion Batteries: The Incumbent Technology. *BloombergNEF* **2019**, *1*, 1–21.
- (6) Zhou, G.; Li, F.; Cheng, H. M. Progress in Flexible Lithium Batteries and Future Prospects. *Energy Environ. Sci.* **2014**, *7* (4), 1307–1338. <https://doi.org/10.1039/c3ee43182g>.
- (7) Wang, Y.; Yi, J.; Xia, Y. Recent Progress in Aqueous Lithium-Ion Batteries. *Adv. Energy Mater.* **2012**, *2* (7), 830–840. <https://doi.org/10.1002/aenm.201200065>.
- (8) Etacheri, V.; Marom, R.; Elazari, R.; Salitra, G.; Aurbach, D. Challenges in the Development of Advanced Li-Ion Batteries: A Review. *Energy Environ. Sci.* **2011**, *4* (9), 3243–3262. <https://doi.org/10.1039/c1ee01598b>.
- (9) Lu, J.; Li, Y.; Fu, J.; Amine, K.; Zhong, C.; Chen, Z.; Hu, W.; Wu, T. Recent Advances in Flexible Zinc-Based Rechargeable Batteries. *Adv. Energy Mater.* **2018**, *9* (1), 1802605. <https://doi.org/10.1002/aenm.201802605>.
- (10) Heller, A. Potentially Implantable Miniature Batteries. *Anal. Bioanal. Chem.* **2006**, *385* (3), 469–473. <https://doi.org/10.1007/s00216-006-0326-4>.
- (11) Song, M.; Tan, H.; Chao, D.; Fan, H. J. Recent Advances in Zn-Ion Batteries. *Adv. Funct. Mater.* **2018**, *28* (41), 1–27. <https://doi.org/10.1002/adfm.201802564>.
- (12) Wang, F.; Hu, E.; Sun, W.; Gao, T.; Ji, X.; Fan, X.; Han, F.; Yang, X. Q.; Xu, K.; Wang, C. A Rechargeable Aqueous Zn<sup>2+</sup>-Battery with High Power Density and a Long Cycle-Life. *Energy Environ. Sci.* **2018**, *11* (11), 3168–3175. <https://doi.org/10.1039/c8ee01883a>.
- (13) Pan, H.; Shao, Y.; Yan, P.; Cheng, Y.; Han, K. S.; Nie, Z.; Wang, C.; Yang, J.; Li, X.; Bhattacharya, P.; Mueller, K. T.; Liu, J. Reversible Aqueous Zinc/Manganese Oxide Energy Storage from Conversion Reactions. *Nat. Energy* **2016**, *1* (April), 1–7. <https://doi.org/10.1038/nenergy.2016.39>.
- (14) Zhang, N.; Cheng, F.; Liu, J.; Wang, L.; Long, X.; Liu, X.; Li, F.; Chen, J. Rechargeable Aqueous Zinc-MaZhang, N., Cheng, F., Liu, J., Wang, L., Long, X., Liu, X., ... Chen, J. (2017). Rechargeable Aqueous Zinc-Manganese Dioxide Batteries with High Energy and Power Densities. *Nature Communications*, *8*(1), 1–9. <https://doi.org/10.1038/s41467-017-00467-x>.
- (15) Wang, L.; Huang, K. W.; Chen, J.; Zheng, J. Ultralong Cycle Stability of Aqueous Zinc-Ion Batteries with Zinc Vanadium Oxide Cathodes. *Sci. Adv.* **2019**, *5* (10), 1–11. <https://doi.org/10.1126/sciadv.aax4279>.
- (16) Li, J.; Mccoll, K.; Lu, X.; Sathasivam, S.; Dong, H.; Kang, L.; Li, Z.; Zhao, S.; Kafizas, G.; Wang, R.; Brett, D. J. L.; Shearing, P. R.; Corà, F.; He, G.; Carmalt, C. J.; Ivan, P. Materials in Aqueous Zinc-Ion Batteries. **2020**, *2000058*, 0–48. <https://doi.org/10.1002/aenm.202000058>.
- (17) Yang, Y.; Tang, Y.; Fang, G.; Shan, L.; Guo, J.; Zhang, W.; Wang, C.; Wang, L.; Zhou, J.; Liang, S. Li<sup>+</sup> Intercalated V<sub>2</sub>O<sub>5</sub>·nH<sub>2</sub>O with Enlarged Layer Spacing and Fast Ion Diffusion as an Aqueous Zinc-Ion Battery Cathode. *Energy Environ. Sci.* **2018**, *11* (11), 3157–3162. <https://doi.org/10.1039/c8ee01651h>.
- (18) Ma, L.; Chen, S.; Long, C.; Li, X.; Zhao, Y.; Liu, Z.; Huang, Z.; Dong, B.; Zapien, J. A.; Zhi, C. Achieving High-Voltage and High-Capacity Aqueous Rechargeable Zinc Ion Battery by Incorporating Two-Species Redox Reaction. *Adv. Energy Mater.* **2019**, *9* (19), 1902446, 1–10. <https://doi.org/10.1002/aenm.201902446>.
- (19) Zhang, L.; Chen, L.; Zhou, X.; Liu, Z. Towards High-Voltage Aqueous Metal-Ion Batteries beyond 1.5 V: The Zinc/Zinc Hexacyanoferrate System. *Adv. Energy Mater.* **2015**, *5* (2), 1–5. <https://doi.org/10.1002/aenm.201400930>.
- (20) Liang, H.; Cao, Z.; Ming, F.; Zhang, W.; Anjum, D. H.; Cui, Y.; Cavallo, L.; Alshareef, H. N. Aqueous Zinc-Ion Storage in MoS<sub>2</sub> by Tuning the Intercalation Energy. *Nano Lett.* **2019**, *19* (5), 3199–3206. <https://doi.org/10.1021/acs.nanolett.9b00697>.
- (21) Li, H.; McRae, L.; Firby, C. J.; Elezzabi, A. Y. Rechargeable Aqueous Electrochromic Batteries Utilizing Ti-Substituted Tungsten Molybdenum Oxide Based Zn<sup>2+</sup> Ion Intercalation Cathodes. *Adv. Mater.* **2019**, *31* (15), 1–9. <https://doi.org/10.1002/adma.201807065>.
- (22) He, X.; Zhang, H.; Zhao, X.; Zhang, P.; Chen, M.; Zheng, Z.; Han, Z.; Zhu, T.; Tong, Y.; Lu, X. Stabilized Molybdenum Trioxide Nanowires as Novel Ultrahigh-Capacity Cathode for Rechargeable Zinc Ion Battery. *Adv. Sci.* **2019**, *6* (14), 2–9. <https://doi.org/10.1002/advs.201900151>.
- (23) Zhao, Q.; Huang, W.; Luo, Z.; Liu, L.; Lu, Y.; Li, Y.; Li, L.; Hu, J.; Ma, H.; Chen, J. High-Capacity Aqueous Zinc Batteries Using Sustainable Quinone Electrodes. *Sci. Adv.* **2018**, *4* (3), 1761. <https://doi.org/10.1126/sciadv.aao1761>.
- (24) Kundu, D.; Oberholzer, P.; Glaros, C.; Bouzid, A.; Tervoort, E.; Pasquarello, A.; Niederberger, M. Organic Cathode for Aqueous Zn-Ion Batteries: Taming a Unique Phase Evolution toward Stable Electrochemical Cycling. *Chem. Mater.* **2018**, *30* (11), 3874–3881. <https://doi.org/10.1021/acs.chemmater.8b01317>.
- (25) Wang, J.; Wang, J. G.; Qin, X.; Wang, Y.; You, Z.; Liu, H.; Shao, M. Superfine MnO<sub>2</sub> Nanowires with Rich Defects Toward Boosted Zinc Ion Storage Performance. *ACS Appl. Mater. Interfaces* **2020**, *12* (31), 34949–34958. <https://doi.org/10.1021/acsami.0c08812>.
- (26) Wang, J.; Wang, J. G.; Liu, H.; Wei, C.; Kang, F. Zinc Ion Stabilized MnO<sub>2</sub> Nanospheres for High Capacity and Long Lifespan Aqueous Zinc-Ion Batteries. *J. Mater. Chem. A* **2019**, *7* (22), 13727–13735. <https://doi.org/10.1039/c9ta03541a>.
- (27) Wang, J.; Wang, J. G.; Liu, H.; You, Z.; Wei, C.; Kang, F. Electrochemical Activation of Commercial MnO Microsized Particles for High-Performance Aqueous Zinc-Ion Batteries. *J. Power Sources* **2019**, *438* (August), 226951. <https://doi.org/10.1016/j.jpowsour.2019.226951>.
- (28) Guo, S.; Liang, S.; Zhang, B.; Fang, G.; Ma, D.; Zhou, J. Cathode Interfacial Layer Formation via in Situ Electrochemically Charging in Aqueous Zinc-Ion Battery. *ACS Nano* **2019**, *13* (11), 13456–13464. <https://doi.org/10.1021/acsnano.9b07042>.

- (29) Karan, S.; Sahu, T. B.; Sahu, M.; Mahipal, Y. K.; Agrawal, R. C. Characterization of Ion Transport Property in Hot-Press Cast Solid Polymer Electrolyte (SPE) Films: [PEO: Zn(CF<sub>3</sub>SO<sub>3</sub>)<sub>2</sub>]. *Ionics (Kiel)*. **2017**, *23* (10), 2721–2726. <https://doi.org/10.1007/s11581-017-2036-7>.
- (30) Kumar, G. G.; Sampath, S. Electrochemical Characterization of Poly(Vinylidene fluoride)-Zinc Triflate Gel Polymer Electrolyte and Its Application in Solid-State Zinc Batteries. *Solid State Ionics* **2003**, *160* (3–4), 289–300. [https://doi.org/10.1016/S0167-2738\(03\)00209-1](https://doi.org/10.1016/S0167-2738(03)00209-1).
- (31) Girish Kumar, G.; Sampath, S. Spectroscopic Characterization of a Gel Polymer Electrolyte of Zinc Triflate and Polyacrylonitrile. *Polymer (Guildf)*. **2004**, *45* (9), 2889–2895. <https://doi.org/10.1016/j.polymer.2004.02.053>.
- (32) Yu, M.; Zeng, Y.; Zhang, X.; Wu, Y.; Lu, X.; Yi, J.; Tong, Y.; Meng, Y. Achieving Ultrahigh Energy Density and Long Durability in a Flexible Rechargeable Quasi-Solid-State Zn-MnO<sub>2</sub> Battery. *Adv. Mater.* **2017**, *29* (26), 1700274. <https://doi.org/10.1002/adma.201700274>.
- (33) Long, L.; Wang, S.; Xiao, M.; Meng, Y. Polymer Electrolytes for Lithium Polymer Batteries. *J. Mater. Chem. A* **2016**, *4* (26), 10038–10039. <https://doi.org/10.1039/c6ta02621d>.
- (34) Wu, K.; Huang, J.; Yi, J.; Liu, X.; Liu, Y.; Wang, Y.; Zhang, J.; Xia, Y. Recent Advances in Polymer Electrolytes for Zinc Ion Batteries: Mechanisms, Properties, and Perspectives. *Adv. Energy Mater.* **2020**, *1903977*, 1–32. <https://doi.org/10.1002/aenm.201903977>.
- (35) Xue, Z.; He, D.; Xie, X. Poly(Ethylene Oxide)-Based Electrolytes for Lithium-Ion Batteries. *J. Mater. Chem. A* **2015**, *3* (38), 19218–19253. <https://doi.org/10.1039/c5ta03471j>.
- (36) Manthiram, A.; Yu, X.; Wang, S. Lithium Battery Chemistries Enabled by Solid-State Electrolytes. *Nat. Rev. Mater.* **2017**, *2* (4), 1–16. <https://doi.org/10.1038/natrevmats.2016.103>.
- (37) Li, H.; Han, C.; Huang, Y.; Huang, Y.; Zhu, M.; Pei, Z.; Xue, Q.; Wang, Z.; Liu, Z.; Tang, Z.; Wang, Y.; Kang, F.; Li, B.; Zhi, C. An Extremely Safe and Wearable Solid-State Zinc Ion Battery Based on a Hierarchical Structured Polymer Electrolyte. *Energy Environ. Sci.* **2018**, *11* (4), 941–951. <https://doi.org/10.1039/c7ee03232c>.
- (38) Zhang, S.; Yu, N.; Zeng, S.; Zhou, S.; Chen, M.; Di, J.; Li, Q. An Adaptive and Stable Bio-Electrolyte for Rechargeable Zn-Ion Batteries. *J. Mater. Chem. A* **2018**, *6* (26), 12237–12243. <https://doi.org/10.1039/c8ta04298e>.
- (39) Huang, Y.; Liu, J.; Zhang, J.; Jin, S.; Jiang, Y.; Zhang, S.; Li, Z.; Zhi, C.; Du, G.; Zhou, H. Flexible Quasi-Solid-State Zinc Ion Batteries Enabled by Highly Conductive Carrageenan Bio-Polymer Electrolyte. *RSC Adv.* **2019**, *9* (29), 16313–16319. <https://doi.org/10.1039/c9ra01120j>.
- (40) Liu, Z.; Huang, Y.; Huang, Y.; Yang, Q.; Li, X.; Huang, Z.; Zhi, C. Voltage Issue of Aqueous Rechargeable Metal-Ion Batteries. *Chemical Society Reviews*. Royal Society of Chemistry **2020**, pp 180–232. <https://doi.org/10.1039/c9cs00131j>.
- (41) Zhang, C.; Holoubek, J.; Wu, X.; Daniyar, A.; Zhu, L.; Chen, C.; Leonard, D. P.; Rodríguez-Pérez, I. A.; Jiang, J. X.; Fang, C.; Ji, X. A ZnCl<sub>2</sub> Water-in-Salt Electrolyte for a Reversible Zn Metal Anode. *Chem. Commun.* **2018**, *54* (100), 14097–14099. <https://doi.org/10.1039/c8cc07730d>.
- (42) Wang, F.; Borodin, O.; Gao, T.; Fan, X.; Sun, W.; Han, F.; Faraone, A.; Dura, J. A.; Xu, K.; Wang, C. Highly Reversible Zinc Metal Anode for Aqueous Batteries. *Nat. Mater.* **2018**, *17* (6), 543–549. <https://doi.org/10.1038/s41563-018-0063-z>.
- (43) Zhang, T.; Tang, Y.; Guo, S.; Cao, X.; Pan, A.; Fang, G.; Zhou, J.; Liang, S. Fundamentals and Perspectives in Developing Zinc-Ion Battery Electrolytes: A Comprehensive Review. *Energy Environ. Sci.* **2020**. <https://doi.org/10.1039/d0ee02620d>.
- (44) Huang, J.; Zhou, J.; Liang, S. Guest Pre-Intercalation Strategy to Boost the Electrochemical Performance of Aqueous Zinc-Ion Battery Cathodes. *Acta Phys. Chim. Sin.* **2020**, *0* (0), 2005020–0. <https://doi.org/10.3866/PKU.WHXB202005020>.
- (45) Wang, P.; Shi, X.; Wu, Z.; Guo, S.; Zhou, J.; Liang, S. Layered Hydrated Vanadium Oxide as Highly Reversible Intercalation Cathode for Aqueous Zn-ion Batteries. *Carbon Energy* **2020**, *2* (2), 294–301. <https://doi.org/10.1002/cey2.39>.
- (46) Guo, S.; Qin, L.; Zhang, T.; Zhou, M.; Zhou, J.; Fang, G.; Liang, S. Fundamentals and Perspectives of Electrolyte Additives for Aqueous Zinc-Ion Batteries. *Energy Storage Mater.* **2021**, *34* (October 2020), 545–562. <https://doi.org/10.1016/j.ensm.2020.10.019>.
- (47) Zhang, T.; Tang, Y.; Fang, G.; Zhang, C.; Zhang, H.; Guo, X.; Cao, X.; Zhou, J.; Pan, A.; Liang, S. Electrochemical Activation of Manganese-Based Cathode in Aqueous Zinc-Ion Electrolyte. *Adv. Funct. Mater.* **2020**, *30* (30). <https://doi.org/10.1002/adfm.202002711>.
- (48) Kundu, D.; Hosseini Vajargah, S.; Wan, L.; Adams, B.; Prendergast, D.; Nazar, L. F. Aqueous: Vs. Nonaqueous Zn-Ion Batteries: Consequences of the Desolvation Penalty at the Interface. *Energy Environ. Sci.* **2018**, *11* (4), 881–892. <https://doi.org/10.1039/c8ee00378e>.
- (49) Tang, Y.; Liu, C.; Zhu, H.; Xie, X.; Gao, J.; Deng, C.; Han, M.; Liang, S.; Zhou, J. Ion-Confinement Effect Enabled by Gel Electrolyte for Highly Reversible Dendrite-Free Zinc Metal Anode. *Energy Storage Mater.* **2020**, *27* (November 2019), 109–116. <https://doi.org/10.1016/j.ensm.2020.01.023>.
- (50) Idota, Y.; Kogure, Y.; Kato, T.; Yano, K.; Arakawa, H.; Miyajima, C.; Kasahara, F.; Ogihara, T. Relationship between Physical Parameters of Various Metal Ions and Binding Affinity for Alginate. *Biol. Pharm. Bull.* **2016**, *39* (11), 1893–1896. <https://doi.org/10.1248/bpb.b16-00127>.
- (51) Feng, Y.; Zhang, Q.; Liu, S.; Liu, J.; Tao, Z.; Chen, J. A Novel Aqueous Sodium-Manganese Battery System for Energy Storage. *J. Mater. Chem. A* **2019**, *7* (14), 8122–8128. <https://doi.org/10.1039/c9ta00474b>.
- (52) Wang, D.; Wang, L.; Liang, G.; Li, H.; Liu, Z.; Tang, Z.; Liang, J.; Zhi, C. A Superior δ-MnO<sub>2</sub> Cathode and a Self-Healing Zn-δ-MnO<sub>2</sub> Battery. *ACS Nano* **2019**, *13* (9), 10643–10652. <https://doi.org/10.1021/acs.nano.9b04916>.
- (53) Sun, J. Y.; Zhao, X.; Illeperuma, W. R. K.; Chaudhuri, O.; Oh, K. H.; Mooney, D. J.; Vlassak, J. J.; Suo, Z. Highly Stretchable and Tough Hydrogels. *Nature* **2012**, *489* (7414), 133–136. <https://doi.org/10.1038/nature11409>.
- (54) Qian, H.; Greenhalgh, E. S.; Shaffer, M. S. P.; Bismarck, A. Carbon Nanotube-Based Hierarchical Composites: A Review. *J. Mater. Chem.* **2010**, *20* (23), 4751–4762. <https://doi.org/10.1039/c000041h>.
- (55) Bender, D.; Schuster, J.; Heider, D. Flow Rate Control during Vacuum-Assisted Resin Transfer Molding (VARTM) Processing. *Compos. Sci. Technol.* **2006**, *66* (13), 2265–2271. <https://doi.org/10.1016/j.compscitech.2005.12.008>.

Table Of Content

